Distorted Square Nets of Tellurium in the Novel Quaternary Polytelluride $K_{0.33}Ba_{0.67}AgTe_2$

Xiang Zhang,[†] Jing Li,[†,⊥] Brendan Foran,[‡] Stephen Lee,[*,‡] Hong-You Guo,[†]
Tim Hogan,[§] Carl R. Kannewurf,[§] and Mercouri G. Kanatzidis[*,†]

Contribution from the Department of Chemistry, Michigan State University, East Lansing, Michigan 48824, Department of Chemistry, University of Michigan, Ann Arbor, Michigan 48109, and Department of Electrical Engineering and Computer Science, Northwestern University, Evanston, Illinois 60208

Received April 24, 1995[®]

Abstract: The synthesis, structure, and band structure analysis of the quaternary compound $K_{0.33}Ba_{0.67}AgTe_2$ are reported. Crystals of $K_{0.33}Ba_{0.67}AgTe_2$ were obtained in a $K_2Te/BaTe/Te$ flux by the reaction of 1 mmol of K_2Te, 0.5 mmol of BaTe, 0.5 mmol of Ag, and 4 mmol of Te in an evacuated Pyrex tube at 450 °C for 3 days followed by a slow cooling to 150 °C. The compound has a substructure in the tetragonal space group $I4/mmm$ (no. 139) with $a_{sub} = 4.624(2)$ Å, $c_{sub} = 23.326(4)$ Å, $V = 498.7(3)$ Å^3, at 20 °C (Mo Kα radiation): $Z = 4$, $D_{calc} = 6.23$ g/cm^3, $2\theta_{max} = 50°$, data collected: 592, independent data: 172, observed with $I > 3\sigma(I)$: 108, variables: 13, final $R = 0.054$, $R_w = 0.067$. $K_{0.33}Ba_{0.67}AgTe_2$ has a lamellar structure related to that of $Na_{1.9}Cu_2Se_2 \cdot Cu_2O$. The substructure contains a readily recognizable $[Te_2]^{4/3-}$ square net. The closest Te—Te distance in the net is 3.269(2) Å, not a full covalent bond, but too short for a simple van der Waals contact. While it is predicted that the square $[Te_2]^{4/3-}$ net has metallic properties, the experimental data show a semiconductor behavior which has its origins in a structural distortion. Electron diffraction measurements reveal the presence of two different but related superstructures; an incommensurate orthorhombic superstructure of the tetragonal cell with $a_{super} = 2.84a_{sub}$, $b_{super} = b_{sub}$, and $c_{super} = c_{sub}$, and a commensurate tetragonal superstructure with $a_{super} = 3a_{sub}$, $b_{super} = 3b_{sub}$, and $c_{super} = c_{sub}$. Both extended-Hückel and Hückel calculations suggest that this distortion is a charge density wave. In the case of the incommensurate cell, the theoretically predicted supercell corresponds to the experimentally observed. We also used the μ_2-scaled Hückel method to predict the actual atomic positions within the supercell. The theoretically predicted superstructures have calculated diffraction patterns similar to the experimentally observed ones.

Introduction

Square nets of elements are common in many high symmetry solid-state compounds. Examples include the Cu_2Sb structures,[1] the related ZrSiSe structures,[2] the PbO and anti-PbO structures,[3] the $ThCr_2Si_2$[4] structures, and some other less popular structure types.[5] In these structures, either a transition metal and/or a main group element form some kind of extended planar square net. The chemical, physical, and electronic properties of these compounds are largely decided by these square nets and by their interactions with the remaining part of the structure. Although hundreds of such structures have been reported to-date, only a few are known for tellurium, e.g., the binary rare-earth tellurides, $LnTe_2$, Ln_2Te_5, and $LnTe_3$.[6] In these compounds the Te-nets exhibit significant bonding interactions with the lanthanide. Here, we describe the synthesis, electronic structure studies, and

electrical properties of a novel compound $K_{0.33}Ba_{0.67}AgTe_2$ (**I**), which represents the first quaternary telluride with relatively isolated square-nets of tellurium. We show, using electron-beam and X-ray diffraction experiments and theoretical calculations that the square net possesses a charge density wave.

Experimental Section

Reagents. Chemicals in this work were used as obtained from commercial sources. Alkali and alkaline earth metal tellurides were prepared in liquid ammonia from the metal and tellurium.

Synthesis of $K_{0.33}Ba_{0.67}AgTe_2$ (I). Crystals of $K_{0.33}Ba_{0.67}AgTe_2$ were obtained in a $K_2Te/BaTe/Te$ flux. The reaction of 0.206 g (1 mmol) of K_2Te, 0.132 g (0.5 mmol) of BaTe, 0.054 g (0.5 mmol) of Ag, and 0.510 g (4 mmol) of Te in an evacuated Pyrex tube at 450 °C for 3 days followed by a slow cooling (4°C/h) to 150 °C produced light-brown, thin plates of $K_{0.33}Ba_{0.67}AgTe_2$ in quantitative yield. The product was isolated from the excess flux by dimethylformamide and washed with ether. Microprobe (EDS) analysis on several crystals gave an average ratio of K:Ba:Ag:Te = 1:2:2.9:6.4. Typically, microprobe analysis is accurate to ±5%.

Structure Determination. Powder XRD data were recorded on a calibrated (with FeOCl as internal standard) Philips XRG-3000 computer-controlled powder diffractometer with Ni filtered Cu Kα radiation operating at 35 kV and 35 mA. The homogeneity of the samples was confirmed by comparing the experimental XRD data with its theoretical patterns calculated using the cell parameters and atomic coordinates obtained from the single crystal X-ray structure analysis.

† Michigan State University.
‡ University of Michigan.
§ Northwestern University.
⊥ Permanent address: Department of Chemistry, Rutgers University, Camden, NJ 08102.
® Abstract published in *Advance ACS Abstracts,* September 15, 1995.
(1) Erlander, M.; Hägg, G.; Westgren, A. *Ark. Kemi. Min. Geol.* **1936–38,** *12B,* No. 1.
(2) Haneveld, A. J. K.; Jellinek, F. *Rec. Trav. Chim. Pays-Bas.* **1964,** *883,* 776.
(3) (a) Byström, A. *Ark. Kemi. Min. Geol.* **1945,** *20A,* No. 11. (b) Grønvold, F.; Haraldsen, H.; Vihovde, J. *Acta Chem. Scand.* **1954,** *8,* 1927.
(4) Ban, Z.; Sikirica, M. *Acta Crystallogr.* **1965,** *18,* 594.
(5) (a) LnNi$_2$Si$_3$ (Ln = Sc, U): Kotur, B. Ya; Bodak, O. I.; Gladyshevskii, E. I. *Sov. Phys. Crystallogr.* **1978,** *23,* 101. (b) ScNiSi$_3$: Kotur, B. Ya.; Bodak, O. I.; Mys'kiv, M. G.; Gladyshevskii, E. I. *Sov. Phys. Crystallogr.* **1977,** *22,* 151. (c) SmNiGe$_3$: Bodak, O. I.; Pecharskii, V. K.; Mruz, O. Ya.; Zarodnik, V. Yu.; Vivits'ka, G. M.; Salamakha, P. S. *Dopov. Akad. Nauk. Ukr. RSR, Ser. B* **1985,** *2,* 36.

(6) (a) Lin, W.; Steinfink, H.; Weiss, F. *J. Inorg. Chem.* **1965,** *4,* 877. Wang, R.; Steinfink, H.; Bradley, W. F. *Inorg. Chem.* **1966,** *5,* 142 (b) Pardo, M.-P.; Flahaut, J.; Domange, L. C. R. *Bull. Soc. Chim. Fr.* **1964,** 3267. (c) Ramsey, T. H.; Steinfink, H.; Weiss, E. J. *Inorg. Chem.* **1965,** *4,* 1154.

Table 1. Crystal Data and Details of Structure Determination for $K_{0.33}Ba_{0.67}AgTe_2$

formula	$K_{0.33}Ba_{0.67}AgTe_2$
fw	467.98
$a = b$ (Å)	4.624(2)
c (Å)	23.326(4)
V (Å^3)	498.7(3)
Z	4
T (°C)	20 °C
d_{calc} (g/cm^3)	6.23
$2\theta_{max}$ (deg)	50°
color	brown black
dimensions (mm)	0.15 × 0.10 × 0.005
radiation, λ (Å)	Mo Kα (0.71069 Å)
space group	*I4/mmm* (no. 139)
absorption coeff μ (cm^{-1})	207.9
scan method	$\omega/2\theta$
octants measd	$0{\to}h$, $0{\to}k$, $0{\to}l$ and corresponding Friedel pairs
data collected	592
independent data	172
obsd with $I > 3\sigma(I)$	108
no. of variables	13
R	0.054
R_w	0.067
goodness-of-fit	1.62

$^a R = \Sigma(|F_o| - |F_c|)/\Sigma|F_o|$; $R_w = \{\Sigma w(|F_o| - |F_c|)^2/\Sigma w|F_o|^2\}^{1/2}$.

Single crystal data and details of the data collection and refinement are given in Table 1. A single crystal was placed inside a capillary tube and mounted on a Rigaku AFC6S four-circle diffractometer. Cell parameters were determined from a list of reflections found by an automated search routine. All data were corrected for Lorentz and Polarization effects. No significant intensity decay was observed upon monitoring three check reflections every 150 reflections throughout the data collection. The crystallographic coordinates and equivalent isotropic temperature factors (B_{eq}) of the atoms are given here: Ba, 0, 0, 0.1180(2) and 1.7(1); Te(1), $-1/2$, $-1/2$, 0.1746(1) and 1.6(1); Te-(2), $-1/2$, 0, 0 and 3.1(3); Ag, $-1/2$, 0, 1/4 and 2.2(1); K, 0, 0, 0.1180-(2) and 1.7(1).

All calculations were carried out on a VAXstation 3100/76 computer. The structures were solved straightforwardly by direct methods using SHELXS-86[7] and refined with the TEXSAN[8a] package of crystallographic programs. An empirical absorption correction based on ψ-scans was applied to the data set, followed by a DIFABS[8b] correction to the isotropically refined data. All atoms were eventually refined anisotropically. Final positional and thermal parameters with their estimated standard deviations are given in the supporting information section.

Physical Measurements. Quantitative microprobe analyses were carried out with a JEOL JSM-35C scanning electron microscope (SEM) equipped with a Tracor Northern Energy dispersive spectroscopy (EDS) detector. Standardless analysis was performed, and the average from a number of single crystals was used. Transmission electron microscopy and electron diffraction studies were performed on a JEOL 100CX microscope operating at 100 kV.

UV/visible/near-IR reflectance spectra were measured at room temperature on a Shimadzu UV-3101PC double beam, double monochromator spectrophotometer. Samples were made by grinding the products into fine powders and pressing into thin layers. $BaSO_4$ powder was used as reference (100% reflectance).

Direct current electrical conductivity and thermopower studies were performed on single crystals (approximately 0.5 mm in length). Conductivity measurements were performed in the usual four-probe geometry with 60- and 25$-\mu$m diameter gold wires used for the current and voltage electrodes, respectively. Measurements of the sample cross-sectional area and voltage probe separation were made with a calibrated binocular microscope. Conductivity data were obtained with a
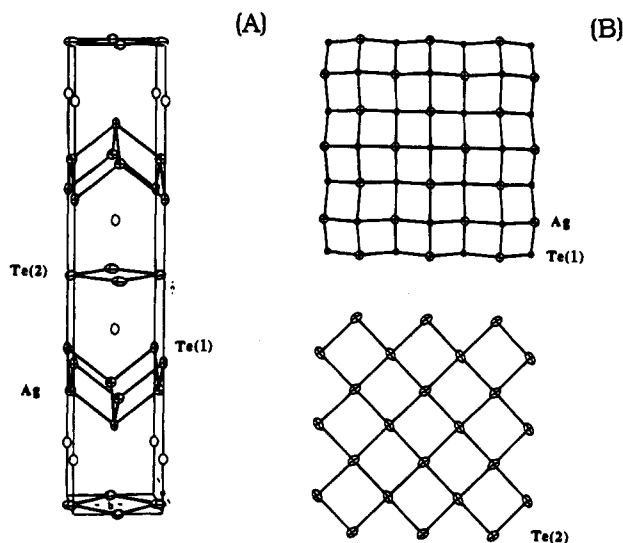
Figure 1. The structure of $K_{0.33}Ba_{0.67}AgTe_2$: (A) the unit cell. Open circles represent K, Ba atoms. (B) Views of the individual $[Ag_2Te_2]^{2-}$ and $[Te_2]^{4/3-}$ layers.

computer-automated system described elsewhere.[9] Thermoelectric power measurements were made by using a slow ac technique[10] which requires the production of a slowly varying periodic temperature gradient across the samples and measuring the resulting sample voltage. Samples were suspended between quartz block heaters by 60$-\mu$m gold wires thermally grounded to the block with GE 7031 varnish. The gold wires were used to support and conduct heat to the sample as well as to measure the voltage across the sample resulting from the applied temperature gradient. The magnitude of the applied temperature gradient was generally 1.0 K. Smaller temperature gradients gave essentially the same results but with somewhat lower sensitivity. In both measurements, the gold electrodes were held in place on the sample with conductive gold paste. Mounted samples were placed under vacuum (10^{-3} Torr) and heated to 320 K for 2$-$4 h to cure the gold contacts. For a variable-temperature run, data (conductivity or thermopower) were acquired during sample warming. The average temperature drift rate during an experiment was kept below 0.3 K/min. Multiple variable-temperature runs were carried out for each sample to ensure reproducibility and stability. At a given temperature, reproducibility was within ±5%.

Results and Discussion

$K_{0.33}Ba_{0.67}AgTe_2$ represents a rather intriguing lamellar structure. Despite its obvious relationship to the $ThCr_2Si_2$[4,11] structure type, the resemblance to $Na_{1.9}Cu_2Se_2 \cdot Cu_2O$[12] is remarkable. The only difference is that the unique $[Cu_2O]$ layer in $Na_{1.9}Cu_2Se_2 \cdot Cu_2O$ is replaced by a tellurium square net in **I**, as shown in Figure 1. The Ag atoms are in $\bar{4}m2$ crystallographic positions and they form a puckered $[Ag_2Te_2]^{2-}$ layer with Te-(1) centered in ($4mm$) sites. This layer is the basic construction unit of any $ThCr_2Si_2$ type structure, with a Ag$-$Te(1) bond length of 2.905(2) Å. Selected distances and angles are given in Table 2.

The most striking feature of this compound is what appears to be a regular $[Te(2)_2]^{4/3-}$ square net made of a monolayer of tellurium atoms. This net forms by the Te(2) atoms in (mmm) positions, with a Te(2)$-$Te(2) distance of 3.269(2) Å, and it is commensurate with the $[Ag_2Te_2]^{2-}$ layer. Although not a full

(7) Sheldrick, G. M. In *Crystallographic Computing* 3; Sheldrick, G. M., Kruger, C., Doddard, R., Eds.; Oxford University Press: Oxford, England, 1985; pp 175$-$189.

(8) (a) TEXSAN: Single Crystal Structure Analysis Software, Version 5.0, (1981). Molecular Structure Corportion, The Woodlands, TX 77381. (b) Walker, N.; Stuart, D. *Acta Crystallogr.* **1983**, *A39*, 158$-$166.

(9) Lyding, J. W.; Marcy, H. O.; Marks, T. J.; Kannewurf, C. R. *IEEE Trans. Instrum. Meas.* **1988**, *37*, 76$-$80.

(10) Marcy, H. O.; Marks, T. J.; Kannewurf, C. R. *IEEE Trans. Instrum. Meas.* **1990**, *39*, 756$-$760.

(11) Hoffmann, R.; Zheng, C. *J. Phys. Chem.* **1985**, *89*, 4175.

(12) Park, Y.; DeGroot, D. C.; Schindler, J. L.; Kannewurf, C. R.; Kanatzidis, M. G. *Chem. Mater.* **1993**, *5*, 8.
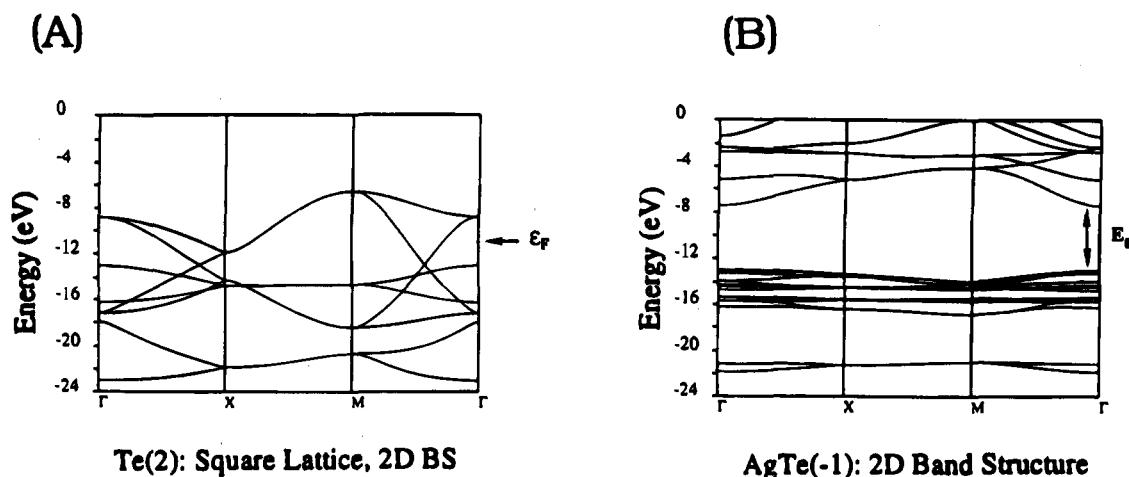
(A)

Te(2): Square Lattice, 2D BS

(B)

AgTe(-1): 2D Band Structure

Figure 2. Band structures for (A) the $[Te_2]^{4/3-}$ net and (B) the two-dimensional $[Ag_2Te_2]^{2-}$ layer. The composite band structure is very much a superposition of the two.

Table 2. Selected Bond Distances (Å) and Angles (deg) in $K_{0.33}Ba_{0.67}AgTe_2$ with Standard Deviations in Parentheses

Ag—Te(1)	2.905(2)	Te(1)—Ag—Te(1)	111.50(6)
		Te(1)—Ag—Te(1)	105.5(1)
Te(2)···Te(2)	3.269(2)	Ag—Te(1)—Ag	105.5(1)
		Ag—Te(1)—Ag	68.50(6)
Ag···Ag	3.269(2)		
Ba(K)—Te(1)	3.526(3)		
Ba(K)—Te(2)	3.594(3)		

covalent bond, the Te(2)—Te(2) distance is too short to be considered as having only van der Waals type interactions (~4.0 Å). Recent work in tellurides has revealed increasing interest in such Te—Te bonds and their importance in affecting the electronic structures of materials.[13,14] Unlike the square nets in most known structures, this square net of tellurium is truly "isolated" from other parts of the structure. The counterions K^+ and Ba^{2+} are the nearest atoms at 3.954(3) Å and are distributed randomly over the same (4mm) site. Occupancy refinement yielded an almost exact ratio of K:Ba = 1:2. If a formal oxidation state of −2 and +1 were assigned to the Te-(1) and Ag in the anti-PbO $[Ag_2Te_2]$ layer respectively, then a −2/3 charge corresponds to each Te(2) in the $[Te_2]^{4/3-}$ square net. Such an assignment is consistent with the longer than normal Te—Te distances in the net. Thermal ellipsoids on Te-(2) sites, however, show distinct elongation along in-plane direction which are parallel to the Te—Te distances. The absence of this ellipsoid asymmetry in the other atomic sites implies the possible presence of a superstructure in the $[Te_2]^{4/3-}$ square net. Recently, two interesting compounds were reported, $RbTe_6$[15] and Cs_3Te_{22},[16] which contain Te-nets different from that described here. The Cs^+ salt contains a $[Te_6]^{3-}$ planar net which, topologically, is derived from a square 4^4 net by removing 2/5 of all the Te atoms.

Several points are noteworthy here in comparison with the Ln_xTe_y phases. The latter contain square nets of tellurium that interact strongly with the neighboring layers,[6a] e.g., the $[NdTe]^+$ layer and other tellurium square nets. The tellurium net in I, however, has no significant covalent interactions with any $[Ag_2-Te_2]$ nor other $[Te_2]$ layers. The Te—Te distances in the square

nets of the Ln_xTe_y range from 3.08 to 3.12 Å, slightly shorter than what we found in I. This could be due to the significant interlayer M—Te interactions (absent in our structure) which funnel some electron density from the Te atoms to the Ln atoms and to steric reasons such as differences in packing requirements between Ln atoms and alkali atoms. In Ln_xTe_y, the square nets primarily account for the metallic behavior.[6a] It has been predicted on theoretical grounds and shown experimentally, that square-chalcogen nets in Ln_xTe_y, $LnSe_2$, $Ln_{10}Se_{19}$, and $RbDy_3$-Se_8 are subject to electronically-driven lattice distortions and site occupancy wave formation (SOW).[14] The latter occurs via ordered chalcogen vacancies. We examined $K_{0.33}Ba_{0.67}AgTe_2$ for similar effects. Occupancy refinement of Te atoms in the square net (or any other atom in the structure) showed that the compound is stoichiometric. Preliminary X-ray photographs (obtained at 23 °C) showed no apparent signs of a superlattice (vide infra).

Charge Transport Properties and Electron Crystallography. We carried out electrical conductivity and thermoelectric power measurements on single crystals of $K_{0.33}Ba_{0.67}AgTe_2$ to confirm the metallic properties suggested for the compound by theoretical band structure calculations. The calculations showed the presence of a Fermi surface in the Te-band associated with the $[Te_2]^{4/3-}$ layers, while the $[Ag_2Te_2]^{2-}$ part of the structure shows a band gap. This suggests that the metallic properties would derive from the Te square net. Surprisingly, data taken from several single crystals indicated a semiconducting behavior, in disagreement with the expected behavior. Figure 3 shows that the electrical conductivity at room temperature is ~0.2 S/cm and drops as the temperature decreases consistent with carrier localization. The slope of the log conductivity vs 1000/T plot gives an activation energy (E_a) of ~0.03 eV. Assuming the data represent the extrinsic region the band-gap (E_g) is estimated to be 0.06 eV. This is consistent with optical absorption measurements which suggest a band gap value <0.15 eV. This semiconductor behavior is confirmed by the thermopower measurements, see Figure 4, which indicate a p-type semiconductor with room temperature Seebeck coefficient of ~200−300 μV/K.

The charge transport results suggest that the compound possesses a band-gap and imply the presence of a structural distortion in the $[Te_2]^{4/3-}$ layers. Since the initial X-ray diffraction results showed no evidence of distortion from the ideal I4/mmm lattice, we examined the $K_{0.33}Ba_{0.67}AgTe_2$ with electron transmission microscopy and namely electron diffraction, given that minor structural distortions in the $[Te_2]^{4/3-}$ layers are expected to be more easily detected by electron rather than by X-ray diffraction.[17]

(13) (a) Canadell, E.; Monconduit, L.; Evain, M.; Brec, R.; Rouxel, J.; Whangbo, M.-H. *Inorg. Chem.* **1993**, *32*, 10. (b) Ansari, M. A.; Bollinger, J. C.; Ibers, J. A. *J. Am. Chem. Soc.* **1993**, *115*, 3838.

(14) (a) Lee, S.; Foran, B. *J. Am. Chem. Soc.* **1994**, *116*, 154. (b) Foran, B.; Lee, S.; Aronson, M. *Chem. Mater.* **1993**, *5*, 974

(15) Sheldrick, W. S.; Schaaf, B. Z. *Naturforsch. B.* **1994**, *49*, 993

(16) Sheldrick, W. S.; Wachhold, M. *Angew. Chem., Int. Ed. Engl.* **1995**, *34*, 450
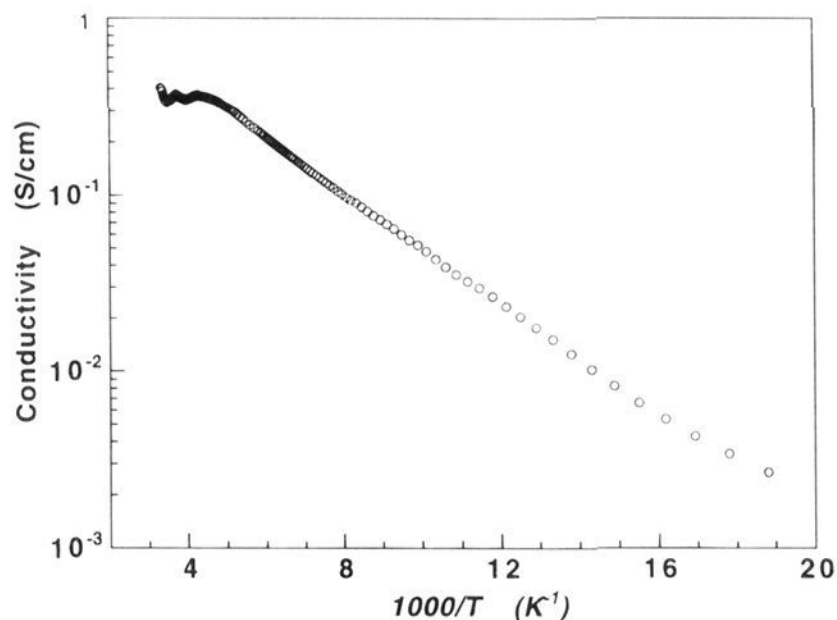
10516 *J. Am. Chem. Soc., Vol. 117, No. 42, 1995*

Zhang et al.

Figure 3. Four-probe variable temperature electrical conductivity data for a single crystal of $K_{0.33}Ba_{0.67}AgTe_2$.

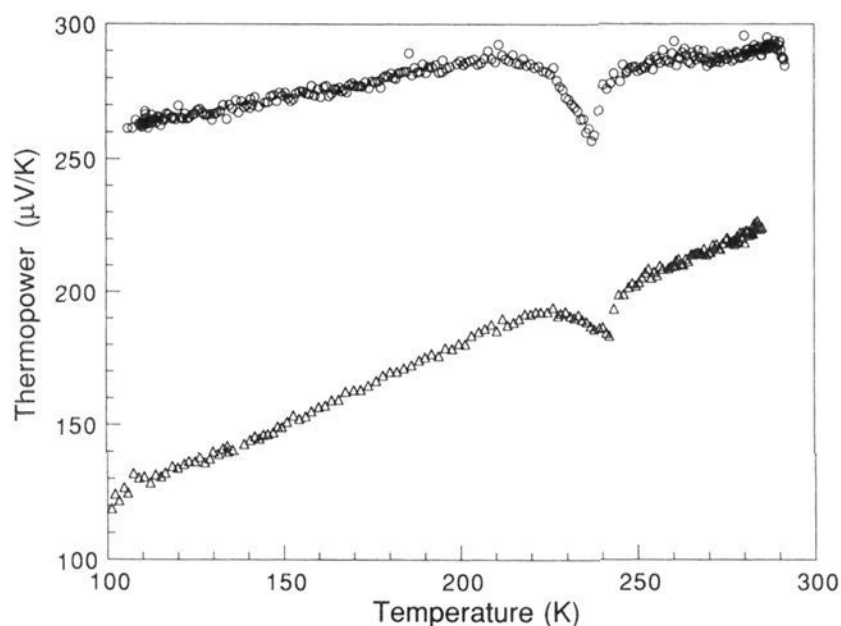**Figure 4.** Variable temperature thermoelectric power data for two single crystals of $K_{0.33}Ba_{0.67}AgTe_2$. The depression exhibited in the data around 240 K is due to an experimental artifact from the measuring apparatus.

Selected area electron diffraction (SAED) with the beam parallel to the [001] zone axis from thin microcrystals of $K_{0.33}Ba_{0.67}AgTe_2$ show clearly the presence of superlattice. Typical selected area electron diffraction patterns showing these two superlattices are shown in Figures 5 and 6. Two different types of crystal domains were found. In the first the material adopts an *incommensurate* lattice distortion with $a^*_{super} = 0.352a^*_{sub}$, $b^*_{super} = b^*_{sub}$, and $c^*_{super} = c^*_{sub}$. Since the $0.352a^*_{sub}$ corresponds to $a_{super} = 2.84a_{sub}$, this superstructure will be referred to as the incommensurate "3 × 1" superlattice. The second crystal domain shows a different but related superlattice where $a_{super} = 3a_{sub}$, $b_{super} = 3b_{sub}$, and $c_{super} = c_{sub}$ (to be referred to as the 3 × 3 superlattice). The tetragonal array of strong reflections, present in both Figures 5 and 6, corresponds to the original subcell. The $[Ag_2Te_2]^{2-}$ part of the structure conforms to the subcell and retains its $4/mmm$ symmetry. The weaker set of reflections in Figure 5, however, appearing at $0.352a^*$ and $0.648a^*$ is due to the orthorhombic incommensurate "3 × 1" superlattice which develops within the $[Te_2]^{4/3-}$ net. The same type of weak reflections is present on Figure 6 as well,

---

(17) Following the electron diffraction study, we re-examined a large number of single crystal samples with X-ray diffraction by obtaining long-exposure (>2 h) axial photographs. This time most, but all, crystals showed very weak reflections at $0.35a^*$ but none along b^*. Nevertheless, we chose electron diffraction as the method of choice because of the higher sensitivity to small structural changes and the ability to examine small specimens and observe different domains.
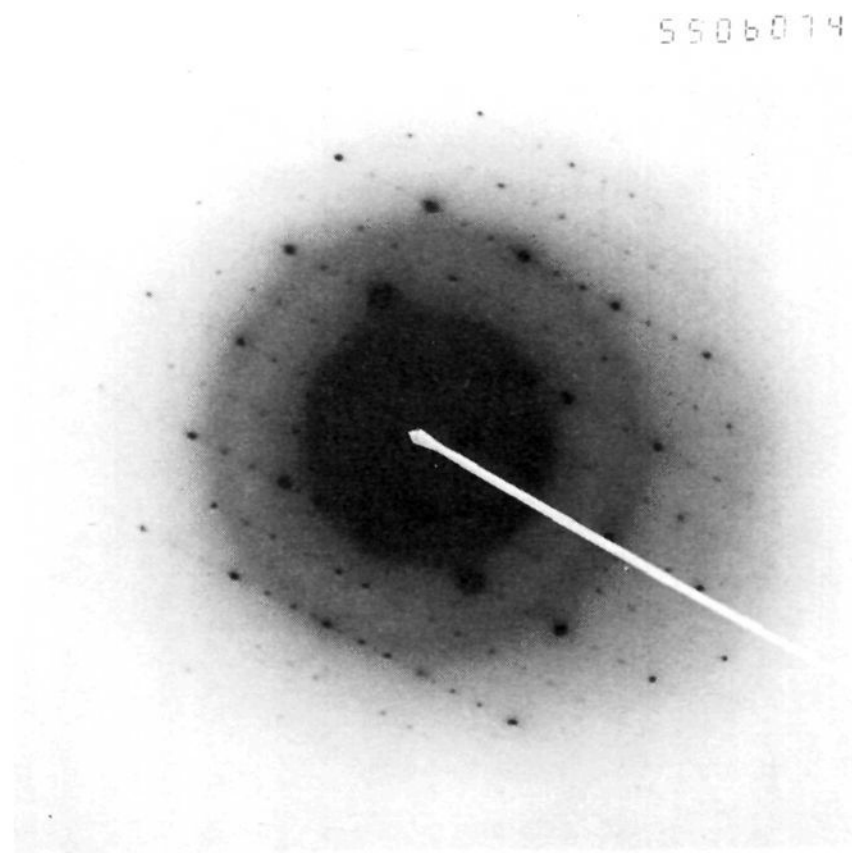

Figure 5. Selected area electron diffraction pattern with the beam parallel to the [001] zone axis from $K_{0.33}Ba_{0.67}AgTe_2$ showing a near tripling of the a axis. The weak spots along the a^*_{sub} direction correspond to $0.352a^*_{sub}$ and are due to an incommensurate "3 × 1" superlattice.
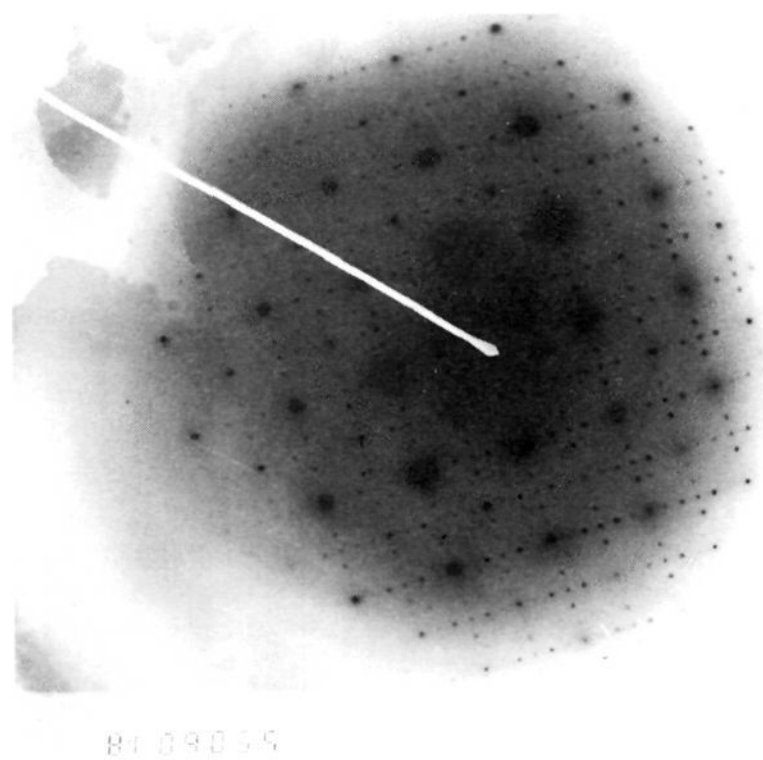

Figure 6. Selected area electron diffraction pattern with the beam parallel to the [001] zone axis from $K_{0.33}Ba_{0.67}AgTe_2$ showing tripling of both a and b axes.

but it occurs along both the a^* and b^* axis of the crystal at $1/3a^*$ and $2/3a^*$ and $1/3b^*$ and $2/3b^*$, respectively. An unusual set of systematic absences occur in this case where in the $hk0$ family, h or $k \neq 3n$. This *commensurate* 3 × 3 superstructure cannot come from micro-twinning of two incommensurate "3 × 1" lattices rotated with respect to each other by 90°.

These results strongly suggest electron *localization* within the $[Te_2]^{4/3-}$ slabs in the form of a charge density wave (CDW). Since the formal negative charge per Te atom is −0.67, it is reasonable to expect that a CDW may exist allowing the formation of discrete Te_3^{2-} units. The interpretation of the electron diffraction data and the rationalization of the two superstructures (3 × 1 and 3 × 3) in the $[Te_2]^{4/3-}$ nets is given below.
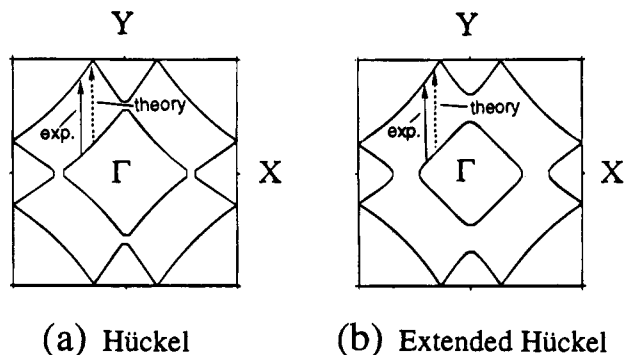
(a) Hückel   (b) Extended Hückel

Figure 7. Hückel and Extended Hückel Fermi surfaces for tellurium square sheet structures showing maximal nesting vector. The theoretical and experimental vectors are identical to the limits of experimental accuracy.

Theoretical Calculations

Maximal Nesting Vector. The two-dimensional character of $K_{0.33}Ba_{0.67}AgTe_2$ as well as the metallic character of the undistorted Te infinite square lattice are both indicators to the potential for (CDW) formation. We therefore calculated the shape of the Fermi surface using Hückel and extended Hückel (eH) band theory.[18] The use of the eH method has recently been demonstrated to provide accurate predictions as well as rationalizations of incipient CDWs.[19] The Hückel Fermi surface is also presented here, since we later use a scaled version of this Hamiltonian for prediction of the actual distortion pattern. In both methods, full three-dimensional band calculations showed that the Fermi surface was dominated by orbitals from the square sheet Te atoms. This is a reasonable result, as these are the only tellurium atoms not fully reduced to the −2 state, and therefore these are the only tellurium atoms for which there are both occupied and unoccupied orbitals. The Fermi surface showed little change in going from three-dimensional calculations of the whole structure to just two-dimensional calculations on isolated Te square sheets. Both Hückel and eH Fermi surfaces share several features in common. In Figure 7 we show the Fermi surfaces for both the Hückel and eH band calculations for a Te square sheet (two Te atoms per unit cell as in the subcell solved by X-rays). For both calculations, the Fermi energy crosses two separate electronic surfaces. The intercept of these surfaces with the Fermi energy is thus the line plotted in Figure 7. For both intercepts, the overall pattern is of two independent sets of diagonal parallel lines. These figures can be used to determine probable distortion modes of $K_{0.33}Ba_{0.67}AgTe_2$. In particular we need to find that vector which connects the maximal portion of the Fermi surface to adjacent portions of this same surface.[19] Such a vector is termed the maximal nesting vector. It corresponds to the vector, in the momentum representation, of the corresponding CDW distortion. Such vectors are particularly significant as they can be directly compared to the new reciprocal lattice vectors found in diffraction studies. In Figure 7 we show the actual maximal nesting vector for $K_{0.33}Ba_{0.67}AgTe_2$. This vector is maximal as it connects both sets of diagonal lines of the Fermi surface to their corresponding diagonal partner. A careful examination of the diagonal lines shows that the seemingly parallel lines of Figure 7 are not exactly parallel. We find in the case of the

extended Hückel calculations that the nesting vector along the indicated direction varies in magnitude from 0.27 to 0.42 reciprocal units (r.u.). For the simple Hückel calculations the magnitude varies from 0.32 to 0.38. The average nesting vector found by both theoretical methods is $0.35a^* + 0.00b^* + 0.00c^*$. The observed CDW discussed in the previous section is $0.352a^* + 0.00b^* + 0.00c^*$. The agreement between theory and experiment is therefore quite good.

Incommensurate 3 × 1 Superlattice Structure. The agreement between maximal nesting vector of the Fermi surface and the observed superstructure, through electron diffraction, strongly suggests that electronic factors in the Te square sheet are responsible for the superlattice distortion. To model this distortion in the atomistic level we decided to use the μ_2-scaled Hückel approach which had previously been shown to give reasonable rationalization of intermetallic structures.[20] In this method one adds to the purely attractive Hückel potential a repulsive potential to ensure an equilibrium geometry of reasonable density. In the spirit of a Morse potential, the repulsive potential is chosen to vary as a square of the attractive potential with respect to overall size. The one additional parameter in this method, which we call the second moment, sets the equilibrium size to that found by experiment. In the case of purely covalent or metallic nets the μ_2-Hückel method is sufficiently accurate that one can couple it to an energetic steepest descent algorithm to find both global and local energy minimum structures.[14a] The μ_2-Hückel method thus produces real space atomistic minima which complement the reciprocal lattice results of nesting vector theory. In the current case there is the added complication that we have an incommensurate CDW of $0.352a^*$. In any finite real space simulation one can only consider true integral supercells (i.e., the supercell must be an integral times the original subcell). We therefore need to find rational approximations of the $0.352a^*$, where the denominator of the rational approximation gives the integer size of the supercell. Small denominator rational approximations include $1/3 = 0.333$, $5/14 = 0.357$, and $6/17 = 0.353$. These approximations correspond to a 3-, 14-, and 17-fold supercell in the a-axis. We are computationally limited to an accurate study of only the smallest of these rational approximations which we denote as the "3 × 1" superlattice structure. The X-ray structure of the subcell showing anomalous Te anisotropic temperature factors, the charge transport data showing a semiconductor, and the maximal Fermi nesting vector study of the previous section all give strong evidence the primary cause of the observed superstructure is a distortion in the Te-square net (as opposed to K and Ba partial or complete ordering). Therefore, starting from random initial variants of just the square lattice of Te atoms, we found a number of optimized minima for the Te square sheet for the 3 × 1 supercell. The two lowest energy solutions of our μ_2-Hückel optimization are illustrated in Figure 8. Both consist of bent Te_3^{2-} trimers. In the lowest energy structure (the global minimum) the trimers are all pointing in the same direction, yielding a C-centered structure. By contrast, in the penultimate energy structure half the trimers point in one direction, while the other trimers point the opposite way in a centrosymmetric fashion. The latter arrangement breaks the C-centering condition found in the global energy minimum.

It is possible to ascribe the stability of the global energy minimum to simple molecular orbital effects. As noted in earlier work,[14a] the principal type of interfragment bonds, such as the

(18) For eH calculations we used the Te parameters found: Canadel, E.; Mathey, Y.; Whangbo, M.-H. *J. Am. Chem. Soc.* **1988**, *110*, 104. For μ_2-Hückel parameters we took $\xi(5s) = 3.13$, $H_{ii}(5s) = -29.5$ eV, $\xi(5p) = 2.16$, $H_{ii}(5s) = -13.2$ eV. For discussions of differences in Hückel and eH parameters see refs 14a and 20d.

(19) Whangbo, M. H.; Canadell, E.; Foury, P.; Pouget, J.-P. *Science* **1991**, *252*, 96. (b) Canadell, E.; Whangbo, M. H. *Chem. Rev.* **1992**, *114*, 965.

(20) (a) Hoistad, L. M.; Lee, S.; Pasternak, J. *J. Am. Chem. Soc.* **1994**, *116*, 4790. (b) Lee, S.; Rousseau, R.; Wells, C.; *Phys. Rev.* **1992**, *46*, 12121. (c) Lee, S. *Acc. Chem. Res.* **1991**, *24*, 249. (d) Lee, S. *J. Am. Chem. Soc.* **1991**, *113*, 8611.
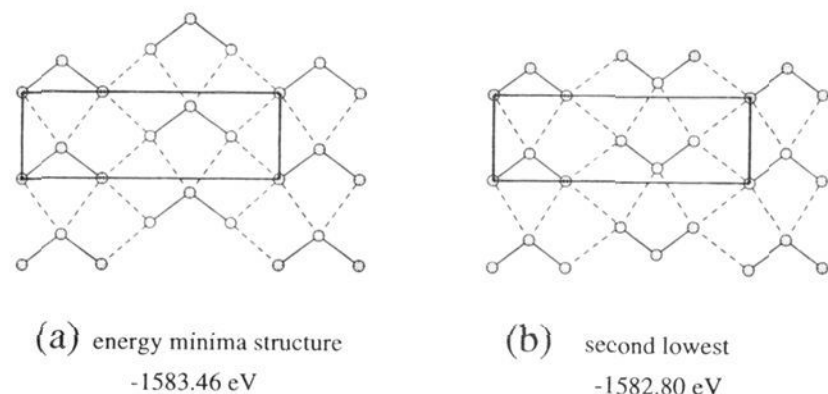
10518   *J. Am. Chem. Soc., Vol. 117, No. 42, 1995*

Zhang et al.

Figure 8. (a) Predicted distortion pattern for $K_{0.33}Ba_{0.67}AgTe_2$ and (b) next lowest energy structure.
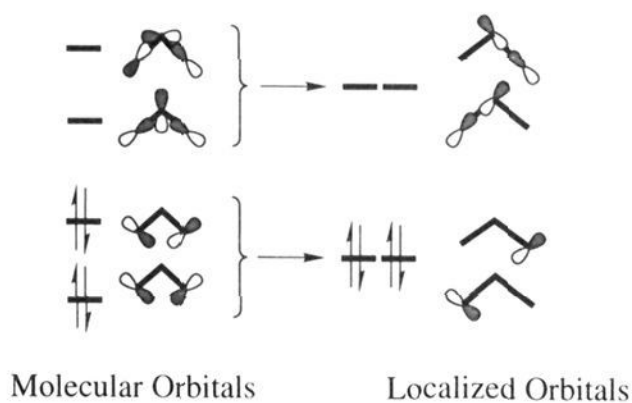

Molecular Orbitals   Localized Orbitals

Figure 9. Construction of localized orbitals from linear combinations of the two highest occupied molecular orbitals and two lowest unoccupied orbitals.
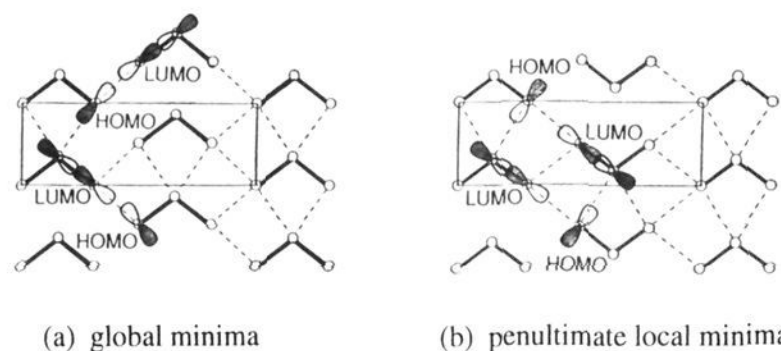

(a) global minima   (b) penultimate local minima

Figure 10. Comparison of HOMO and LUMO orbital interactions between adjacent Te_3^{2-} fragments found in lowest energy structure. In the second lowest energy structure the arrangement of the Te_3^{2-} fragments allows only LUMO-LUMO interactions which cannot be energetically stabilizing.

bonds found between adjacent Te_3^{2-} fragments in the current study, are of Lewis acid-Lewis base type. Particular attention should therefore be paid to the HOMOs and LUMOs of the Te_3^{2-} fragments, shown in Figure 9. It is convenient to take linear combinations of the two HOMOs and the two LUMOs. In this way one generates a localized picture of the HOMOs and LUMOs (much as Wannier orbitals give a localized view of band orbitals for crystals). These are shown in Figure 9. As may be seen in this figure, the LUMOs are σ^* orbitals along each of the two Te—Te bonds found in Te_3^{2-}. The HOMOs are located on outer atom Te p orbitals which are π-orbitals with respect to these σ Te—Te bonds. Maximum interfragment stability is found when the HOMOs of a given Te_3^{2-} trimer point toward the LUMOs of adjacent trimers.[21] In the global minimum energy structure the trimers are oriented in such a way as to maximize such HOMO—LUMO interactions, see Figure 10. By contrast, in the case of the penultimate structure LUMO orbitals are directly pointed to other LUMO orbitals. This difference between HOMO—LUMO and LUMO—LUMO interaction quantitatively accounts for the 0.66 eV difference in energy between the two structures. The actual distortion mode predicted by the μ_2-scaled Hückel approach is the one

(21) Fukui, K. *Acc. Chem. Res.* **1971**, *4*, 57.

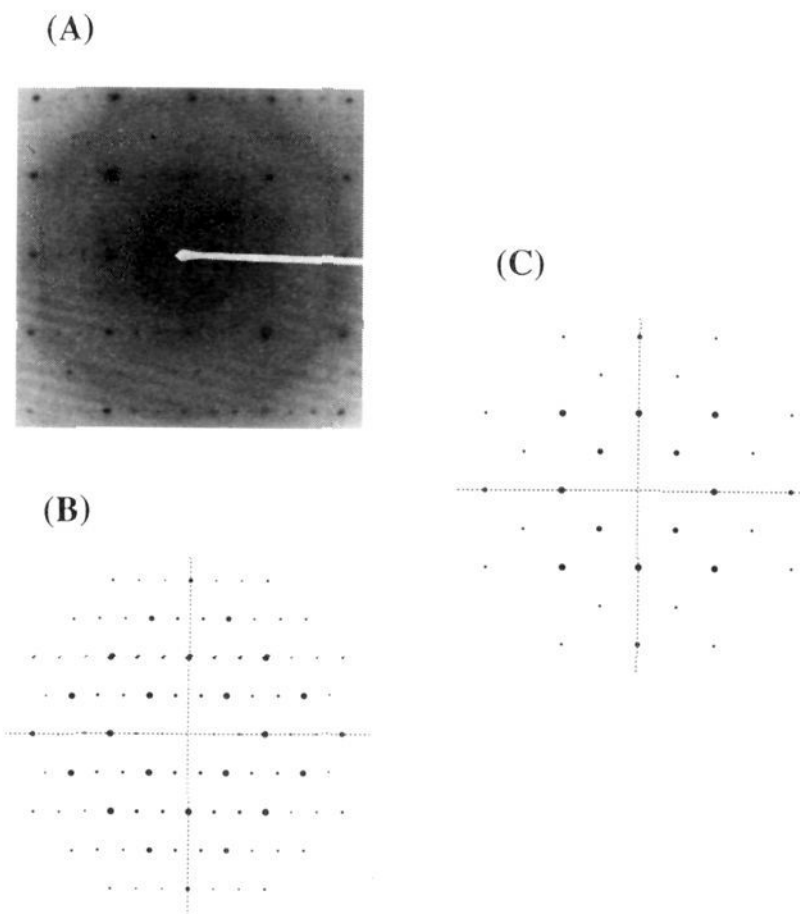**(A)**

(C)

(B)

Figure 11. (a) Selected area electron diffraction pattern with the beam parallel to the [001] zone axis from $K_{0.33}Ba_{0.67}AgTe_2$. (b) Simulated electron diffraction pattern for predicted (3 × 1) lowest energy superlattice. (c) Simulated electron diffraction pattern for the ideal (1 × 1) sublattice.

which maintains maximal Lewis acid—Lewis base interactions between incipient fragments.

In Figure 11 we directly compare simulated diffraction patterns[22] generated from the structure found by the μ_2-Hückel global minimum to the experimentally observed diffraction pattern, as well as the simulated pattern of the original subcell. It must be noted that each unit cell contains two layers of Te_3^{2-} trimers, one at $z = 0$ and one at $z = 1/2$. In the simulation, the two layers can assume several possible orientations relative to each other.

For simulations, we have chosen the two orientations for both the lowest and second lowest minimum structures which give the best agreement with the experimental results. Both minimum energy structures can lead to simulated patterns that are in fair agreement with the experimental pattern. To a large extent, this agreement is controlled by the lattice symmetry of the Te square lattice structure. As we discussed above, the global energy minimum structure has a C-centered arrangement for the distorted Te square lattice. This leads to a systematic extinction law for the superstructure of hkl; $h + k = 2n + 1$. We experimentally observe that the "3 × 1" phase under electron diffraction does indeed have such a C-centering condition. It is this agreement which forces the global energy minimum structure to give rise to the experimentally observed electron diffraction pattern. By contrast, in the penultimate energy structure, a single distorted Te square net has primitive symmetry. For a single layer there is therefore no corresponding extinction law. We have been able to produce a reasonable simulated model for the penultimate structure only by assuming an orientation between the Te square lattices of $z = 0$ and $z = 1/2$ that leads to an overall I-centering for the three-dimensional cell. An I-centered cell has the systematic absence law hkl; $h + k + l = 2n + 1$. For the [001] or $hk0$ plane in the electron

(22) Calculated with the software package CERIUS[2] Chemical Simulations Software Package, Molecular Simulation Inc., Burlington, MA 1994.
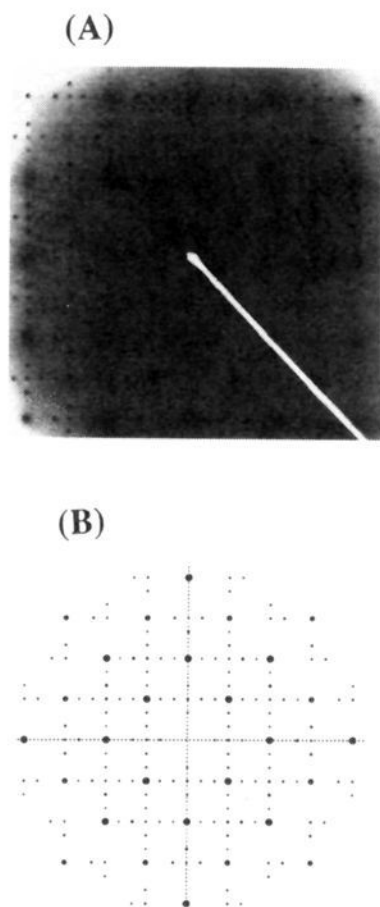
(A)

(B)

Figure 12. (a) Selected area electron diffraction pattern with the beam parallel to the [001] zone axis from $K_{0.33}Ba_{0.67}AgTe_2$ showing the (3 × 3) superlattice. (b) Simulated electron diffraction pattern for predicted (3 × 3) superlattice. In this model the two layers of Te_3^{2-} are rotated by 90°.

diffraction picture, both I- and C-centering overlap in their systematic extinctions.

To distinguish between those two alternative structures, we must, therefore, turn to planes other than the $hk0$ plane. We have undertaken such a study and have examined the [1−3 3] plane. Here one can clearly distinguish between the I- and C-centering laws. The [1−3 3] plane shows reflections consistent with C-centering and not I-centering, thus ruling out the possibility that the penultimate energy structure is responsible for the observed "3 × 1" superlattice.

As a final theoretical study, we considered a 3 × 3 cell where the new reciprocal lattice vectors are $1/3a^*$, $1/3b^*$, and c^* when compared with the original sublattice. This is a fairly large cell, composed of 18 Te atoms. Although we have not been able to study the 3 × 3 cell electronic surface to the same degree as the 3 × 1 cell, our results indicate that the minimum global energy and second lowest energy structures of the 3 × 1 cell are also the stable alternatives for the 3 × 3 cell two-dimensional Te square lattice.

Commensurate 3 × 3 Superlattice. A third possible orientation of the two Te_3^{2-} layers in the cell, relative to each other, is one that disposes the two 2-fold axes of the tritelluride anions in the two layers perpendicularly. This arrangement places the tripled axes of each layer at 90° from one another and results in a 3 × 3 superstructure for the whole compound. Simulations were made using both the (a) minimum calculated energy and (b) next lowest energy pattern shown in Figure 8. Interestingly, the best fit to the observed data was obtained with pattern (b). The simulated electron diffraction pattern in this case is shown in Figure 12 and matches reasonably well the pattern observed in Figure 6. The intensity differences between the calculated and observed diffraction patterns could be due to additional ordering of K and Ba ions, inaccurate estimation of the degree of distortion in the Te_3^{2-} layers, and dynamic scattering effects from the sample. These results suggest that

in the 3 × 3 structure, the second lowest energy distortion pattern is favored. Why this is opposite to the "3 × 1" incommensurate lattice is unclear. The calculated energy difference between lowest and second lowest energy structures is 0.66 eV/unit cell or equivalently 2.5 kcal/square lattice Te atom. This difference is chemically significant; however, it is certainly plausible that other nonelectronic factors could cause the penultimate structure to be the final stable structure. One possible rationalization for the experimental observations is that the two observed superstructures are not true polymorphs but instead represent two slightly different, but experimentally difficult to measure, stoichiometries. If such were the case our theoretical studies suggest that the incommensurate 3 × 1 superlattice lies closer to the reported stoichiometry than the commensurate 3 × 3 superlattice. Finally, we note that attempts to simulate the 3 × 3 pattern with a twinned model (two commensurate 3 × 1 cells rotated by 90°) were not successful. The $hk0$ reflections where $h = 3n$, $k = 3n$ are observed in experiment but must be absent, in twin simulation, see Figure 6.

Band structures were calculated to show if the minimum energy structure should be metallic or semiconducting. An extended Hückel calculation on the distorted cell shows that we should expect the distorted $K_{0.33}Ba_{0.67}AgTe_2$ to be an insulator. For our predicted distortion pattern, with Te−Te distances in the trimers set at 3.0 Å, the band gap calculated is ~2.0 eV. The disagreement with the band gap found by charge transport and by optical reflectance measurements is not surprising, since it is known that extended Hückel calculations incorrectly estimate the band gap energies.[23]

Concluding Remarks

The rigidity and high stability of the $[Ag_2Te_2]^{2-}$ layers coupled with their tetragonal symmetry are probably responsible for the stabilization of $K_{0.33}Ba_{0.67}AgTe_2$. The tetragonal structure, however, forces all the Te_3^{2-} anions to lie flat with equal Te−Te distances throughout the net, an unlikely arrangement which in many ways violates known Te_x^{2-} chemistry. Therefore, the strong tendency for trimer formation acts as an opposing force against the tetragonal symmetry giving rise to the incommensurate CDW. One can envision, that the structure-directing $[M_2Q_2]^{n-}$ (Q = S, Se, Te) layers could be used as a tool for sandwiching between them unusual species which may otherwise be unstable. For example, the unusual fluorite-like $[M_2O_2]^{2+}$ (M = Bi, La, Nd, Cd, Dy) layers were found stabilized between PbO-like $[M'_2Q_2]^{2-}$ (M′ = Cu, Ag; Q = S, Se) layers in a large family of compounds with tetragonal symmetry.[24] This may lead to novel materials with surprising electronic properties. Thus, the presence of well separated polytelluride $[Te_2]^{4/3-}$ layers in $K_{0.33}Ba_{0.67}AgTe_2$ implies that it might be possible to obtain related compounds[25] (e.g. $K_xBa_yAgTe_n$, $n > 2$) with more than one $[Te_2]^{4/3-}$ layer as part of a homologous family. The pursuit of compounds of the type $A_xB_yTe_n$ (A = alkali; B = alkaline earth) is now justified because they may also contain $[Te_x]^{n-}$ layers with varying electron count and other fascinating nonclassical polytellurides. The recent reports of $RbTe_6$ and Cs_3Te_{22} are a step in this direction.

(23) Harrison, W. A. In *Electronic Structure and Properties of Solids*; Dover Publications: Mineola, NY, 1980; Chapter 6.

(24) Kusainova, A. M.; Berdonosov, P. S.; Akselrud, L. G.; Kholodkovskaia, L. N.; Dolgikg, V. A.; Popovkin, B. A. *J. Solid State Chem.* **1994**, *112*, 189.

(25) We also discovered a minor Te-rich phase that appears structurally related to the parent $K_{0.33}Ba_{0.67}AgTe_2$ structure, but with a larger c lattice constant. This leads us to believe that homologous compounds may exist.

Supporting Information Available: Tables of atomic coordinates of all atoms and anisotropic and isotropic thermal parameters of all atoms (1 page); listings of calculated and observed ($10F_o/10F_c$) structure factors for $K_{0.33}Ba_{0.67}AgTe_2$ (1 page). This material is contained in many libraries on microfiche, immediately follows this article in the microfilm version of the journal, can be ordered from the ACS, and can be downloaded from the Internet; see any current masthead page for ordering information and Internet access instructions.

JA951298+